mater.scichina.com link.springer.com

Published online 7 March 2024 | https://doi.org/10.1007/s40843-023-2788-x
Sci China Mater 2024, 67(4): 1340–1347

Efficient red-emitting lead-free cesium-scandium halide perovskite crystals produced *via* Mn^{2+} doping

Mengyan Cao[1], Renfu Li[2*], Zhilin Li[1], Xiujian Zhao[1] and Xiao Gong[1*]

ABSTRACT **Perovskite crystals with high photoluminescence quantum yields can be rapidly synthesized by doping Mn^{2+} into $Cs_2ScCl_5{\cdot}H_2O$ through a facile wet chemistry approach. The quantum yield of the Mn^{2+}-doped perovskite crystals in the red light region is over 12 times higher than that of the host material and nearly 24 times higher than that of pure Mn-based perovskite $CsMnCl_3{\cdot}2H_2O$. Moreover, density functional theory calculations were used to study the orbital hybridization properties of the materials to further investigate their optical properties. After Mn^{2+} doping, the Mn octahedrons separated by the Sc octahedrons can more effectively restrict excitons, which is conducive to the improvement of quantum yields. Compared with the original band gap, a new hybridized orbital attributed to Mn and the host element appears. The doped sample shows an extended absorption and excitation range from the original deep-ultraviolet (UV) absorption to UV and visible absorption. Based on these properties, the Mn^{2+}-doped perovskites are used to prepare efficient white light-emitting diodes excited by a blue chip, showing an excellent color rendering index of 91, which meets the need for future applications in the field of optoelectronics.**

Keywords: PLQY enhancement, Mn^{2+} doping, DFT calculation, white light-emitting diodes

INTRODUCTION

Perovskites have several remarkable physical properties owing to their highly tunable structure, excellent optoelectronic properties, magnetic properties, ferroelectricity, and dielectric properties [1–9]. These diverse physical properties have led to a wide range of applications of perovskites in the fields of displays, solar cells [10–12], light-emitting diodes (LEDs) [13–16], photodetectors, and lasers. Metal halide perovskites have received increased attention from researchers in recent decades. To solve the toxicity and stability problems caused by lead, other metal elements (such as Zr^{4+}, Sn^{4+}, In^{3+}, Bi^{3+}, and Sc^{3+}) have been used to replace lead in perovskite materials [17,18]. These metal halide perovskites possess advantages such as low cost, adjustable spectra, and simple synthesis and exhibit optical properties that are not identical to those of lead-based perovskites [19,20]. Metal-halide perovskites show specific advantages over lead-halide perovskites for LEDs and anticounterfeiting applications owing to their better stability and unique optical properties [21–23].

However, lead-free metal-halide perovskites often exhibit a very low photoluminescence quantum yield (PLQY); for example, it has been reported that the PLQY of $Cs_2ScCl_3{\cdot}H_2O$ is less than 1% [24]. Therefore, effectively enhancing PLQY without sacrificing stability has become a critical challenge. Some organic ion substitutions may increase the optical performance, but often at the cost of loss of stability. Doping atoms into the lattice structure of the host material is a common method that can effectively modulate the relevant optical or electrical properties of the material [25,26]. Several ions (such as Sb^{3+}, Bi^{3+}, Mn^{2+}, and Yb^{3+}) have been reported to improve the PLQY and even become new luminescence centers in the matrix, inducing new optical phenomena in the matrix. The d/d transition within Mn^{2+} can often be an effective luminescence center, producing emission that typically leads to a large Stokes shift, wide emission range, and long lifetime [27–30]. Most studies on Mn^{2+}-doped perovskites have focused only on colloidal nanocrystals [31,32]. Therefore, it is important to investigate the electronic interactions between the host material and the dopant ions in Mn^{2+}-doped all-organic lead-free perovskites after excluding the effect of organic ligands. Moreover, the current research on $Cs_2ScCl_5{\cdot}H_2O$ is scarce, and as an all-inorganic metal-halide perovskite, its advantages in stability are quite obvious. The use of ion doping to effectively improve the optical properties of $Cs_2ScCl_5{\cdot}H_2O$ and study the correlation between fluorescence and structure is essential for subsequent research development.

In this study, a novel all-inorganic perovskite structure, $Cs_2ScCl_5{\cdot}H_2O$, was used as a substrate material and Mn^{2+} doping was employed to enhance the PLQY and improve the optical performance using a facile synthesis method. The PLQY of the perovskite crystals can be remarkably enhanced from less than 1% to 12% in the orange–red luminescent region, resulting in a more than 12-fold enhancement. We also investigated the absorption and emission properties. The introduction of Mn^{2+} can increase the absorption in the near-ultraviolet (UV) and visible (vis) regions of the substrate material, exhibiting the characteristic emission of Mn^{2+} (orange–red regions) when excited. In addition, the prepared materials have excellent stability and the Mn^{2+} ionic compounds have low toxicity. Density functional theory (DFT) calculations were applied to probe the substrate-doped band-gap properties of the prepared materials to have a better understanding of the energy-band structure of the material itself, which is beneficial for the exploration of optical properties. Our study may provide some inspiration for

[1] State Key Laboratory of Silicate Materials for Architectures, Wuhan University of Technology, Wuhan 430070, China
[2] Fujian Institute of Research on the Structure of Matter, Chinese Academy of Sciences, Fuzhou 350002, China
[*] Corresponding authors (emails: lirenfu@fjirsm.ac.cn (Li R); xgong@whut.edu.cn (Gong X))

 © Science China Press 2024

subsequent novel all-inorganic perovskites and may shed some light on the study of the optical principles of doped materials.

EXPERIMENTAL SECTION

Materials

Cesium chloride (CsCl, 99.99% metals basis), scandium(III) oxide (Sc_2O_3, 99.9% metals basis), and manganese chloride tetrahydrate ($MnCl_2{\cdot}4H_2O$, 99.99% metals basis) were taken from Aladdin Reagent Co. Hydrochloric acid (HCl, 37 wt% analytical reagents), and ethanol (EtOH, ⩾99.7%) were supplied by Sinopharm Chemical Reagent Co., Ltd. The green fluorescence powder ($Y_3Al_5O_{12}:Ce^{3+},Ga^{3+}$) was supported by Yantai Shield Co., Ltd. The LED chips (450 nm) were supported by Juhoon Optoelectronics Co., Ltd.

Material characterizations

UV-vis absorption spectra were tested in the UV/VIS/NIR Spectrometer (Lambda 750 S, PerkinElmer, USA). The PL spectra were measured by the time-resolved fluorescence spectrometer (FL3-22, Jobin-Yvon, USA) at room temperature. X-ray diffraction (XRD) spectra were characterized by using the X-ray diffractometer (Empyrean, Holland). The morphologies and the energy-dispersive X-ray spectroscopy (EDS) mapping were registered by a field emission scanning electron microscope (SEM, Zeiss Ultra Plus, Germany). The X-ray photoelectron spectroscopy (XPS) spectra were characterized by Thermo Fisher Scientific ESCALAB 250Xi spectrometer (USA). The temperature-dependent PL spectra were taken by using Edinburgh Instruments FLS1000 spectrophotometer with a temperature interval of 80 to 305 K. Excitation light was from the optical parametric amplifier (Orpheus, Light Conversion, Lithuania) pumped by the femtosecond laser (Spirit 1040-8W, Spectra-Physics, USA). The quantum yield was tested by Hamamatsu's absolute quantum yield equipment (C9920-02G). The PL spectra of LED were taken by using HAAS-2000 High Accuracy Array Spectroradiometer (Everfine).

Preparation of Mn^{2+}-doped $Cs_2ScCl_5{\cdot}H_2O$

Typically, 0.5 mmol Sc_2O_3 and x mmol (x = 0.005, 0.01, 0.02, 0.03, and 0.05) $MnCl_2{\cdot}4H_2O$ were added in 8 mL hydrochloric acid and stirred at 90°C for 15 min at atmospheric pressure. Then, 2 mmol CsCl was added to the solution and kept stirring for 5 min at 80°C. After the solution was cooled to room temperature, the precipitate was collected and washed three times using methanol. The final sample was obtained by drying at 80°C for 3 h.

Fabrication of the LED device

Typically, we mixed the phosphor with epoxy glue A, added epoxy glue B after a period of time, and then set it on a 450-nm chip. Then the whole LED device was tested after drying at 80°C for 2 h. The WLED powder mixture consists of $CsScCl{\cdot}H_2O:Mn^{2+}$ powder and commercial $Y_3Al_5O_{12}:Ce^{3+},Ga^{3+}$ powder (green phosphor). The commercial green powder and $CsScCl{\cdot}H_2O:Mn^{2+}$ powder were added in a mass ratio of about 1:4. The total mass of phosphor and the mass ratio of UV curing adhesive was about 1:1.

Computational methods

DFT calculations were performed by using the Castep module in the Materials Studio simulation package. The interactions between ion cores and valence electrons were described by the Blochl's all-electron-like projector augmented wave (PAW) method. The generalized gradient approximation (GGA) with the Perdew–Burke–Ernzerhof (PBE) functional was adopted for the exchange-correlation interaction. The kinetic energy cutoff with 520.0 eV, convergence tolerance with 2.0×10^{-6} eV/atom, force tolerance with 0.002 eV $Å^{-1}$, maximum displacement with 0.002 Å, and max stress with 0.1 GPa were adopted in the calculation. In addition, the 3 × 3× 6 k-points within the gamma centered Monkhorst–Pack scheme is used to sample the Brillouin zone for all the structures. The self-consistent field convergence is set to 1×10^{-6} eV/atom.

RESULTS AND DISCUSSION

A facile low temperature (<100°C) preparation method using toxicity solvents and a short reaction time was chosen for synthesizing of $Cs_2ScCl_5{\cdot}H_2O$. The synthesis of samples was rapidly performed within 30 min in an acidic solution and atmospheric pressure. The preparation of $Cs_2ScCl_5{\cdot}H_2O:Mn^{2+}$ does not require a very harsh environment, and only the Mn^{2+} precursors are mixed into the raw material. SEM images of the samples were evaluated to explore the distribution and morphological characteristics of the material, which was octahedral (Fig. S1). EDS elemental mapping of the matrix material is shown in Fig. S2, wherein the distribution of each element is relatively uniform. The doped material (Fig. 1a, b) clearly shows the presence of Cs, Sc, Mn, and Cl, which are also relatively uniformly distributed in the sample, further confirming the successful doping of Mn^{2+} ions. The crystal structure of $Cs_2ScCl_5{\cdot}H_2O$ represents a typical *Pnma* orthorhombic space group, and the lattice structure model is shown in Fig. 1c [24]. There are isolated metal-halide octahedral structures centered on Sc^{3+}, whereas Cs^+ separates the isolated octahedral structures. To further investigate the structure of the synthesized samples, we conducted XRD and compared the results with the simulated XRD data, which are presented in Fig. 1d. The samples prepared by this method exhibited XRD patterns that corresponded one-to-one with the simulated structures, indicating that the samples were successfully synthesized and are also similar to those previously reported [24].

No peaks corresponding to the synthesized raw materials were found in the XRD patterns, indicating that the washing method was highly effective. Additionally, no new peaks appeared after doping with low concentrations of Mn^{2+} (Fig. 2a), which indicated that the Mn^{2+} precursors tended to appear in the form of doping rather than forming new substances when they were added to the synthesis process in low doses. Compared with the host material, the full width at half maximum (FWHM) values of the XRD patterns of the doped samples were not noticeably reduced, and the corresponding crystallinity was not greatly reduced. When the doping concentration increased, an angular shift in the peak value relative to the original sample was found, which is also due to the smaller ionic radius of Mn^{2+} compared with that of Sc^{3+}.

XPS was also used to analyze the constituent elements and valence information in the samples to determine the form in which the doping elements entered the matrix material. The XPS survey spectra of the original and Mn^{2+}-doped samples are shown in Fig. S3 and Fig. 2b, respectively. The peaks at 642.88 and 654.18 eV in the elemental high-resolution XPS spectrum

© Science China Press 2024

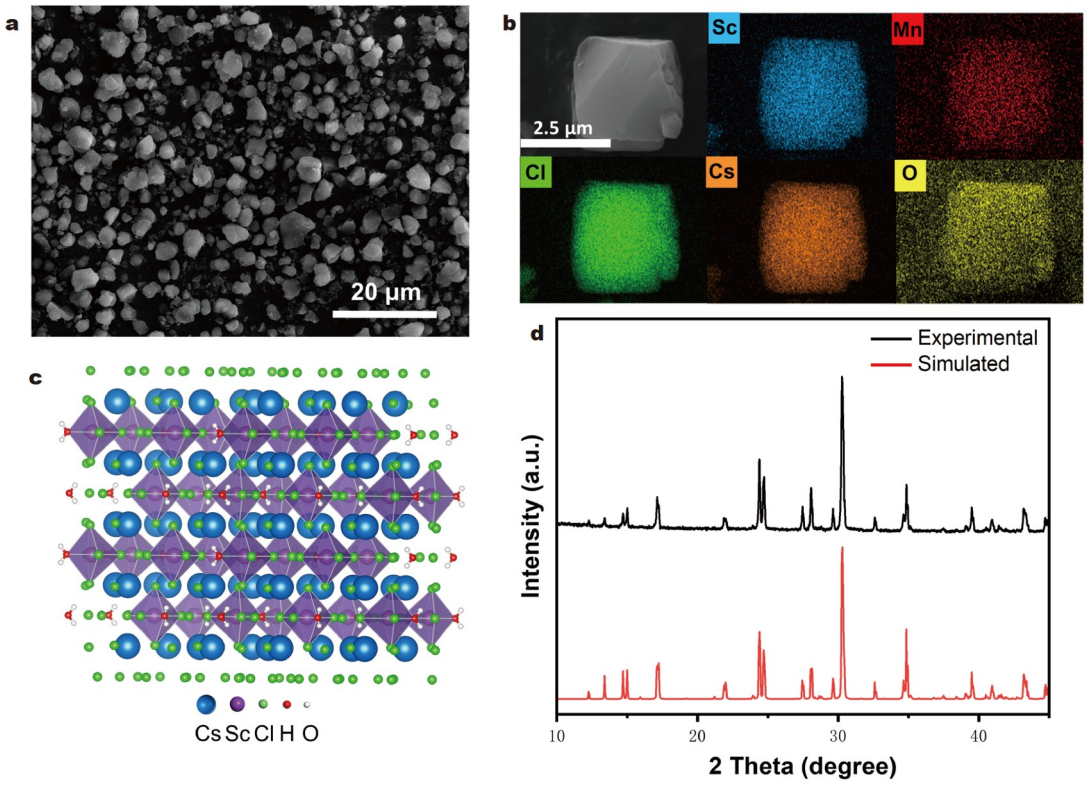

Figure 1 (a) SEM image and (b) EDS elemental mapping of $Cs_2ScCl_5{\cdot}H_2O$:0.03Mn^{2+}. (c) Crystal structure of $Cs_2ScCl_5{\cdot}H_2O$ (blue, Cs; purple, Sc; green, Cl; red, O; white, H). (d) XRD patterns of the simulated and experimental $Cs_2ScCl_5{\cdot}H_2O$ material.

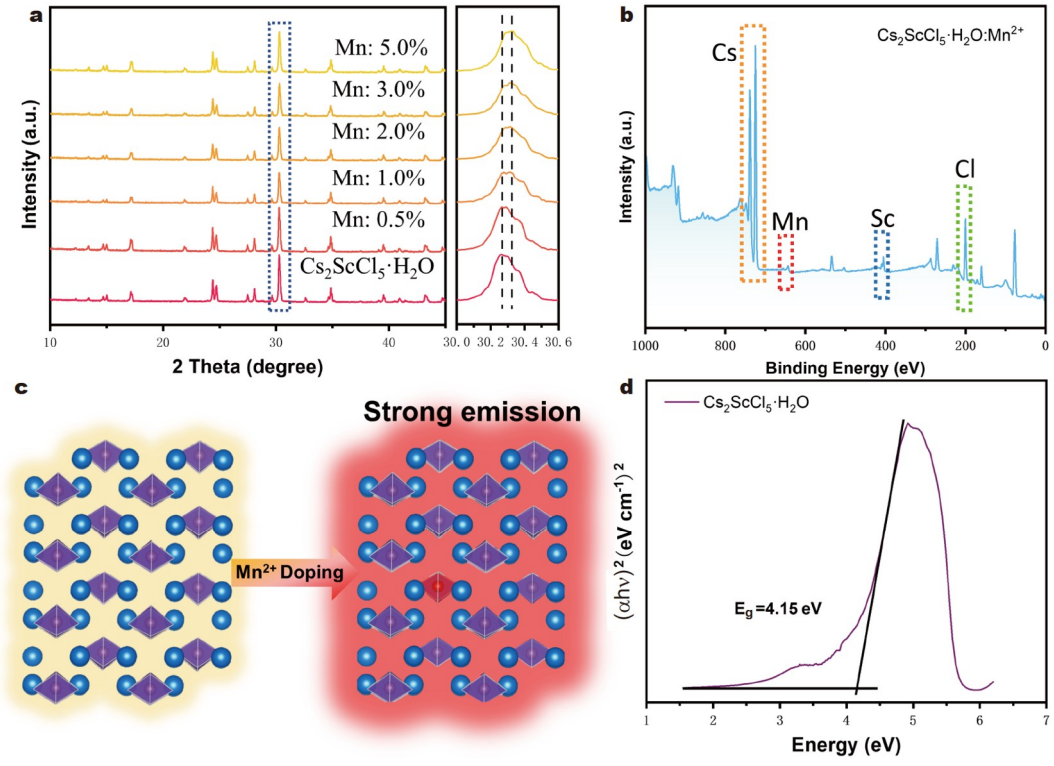

Figure 2 (a) XRD patterns of $Cs_2ScCl_5{\cdot}H_2O$:$x$$Mn^{2+}$ (x = 0.5%–5%), where x refers to the ratio of the doped material to the host material. (b) XPS survey spectrum of $Cs_2ScCl_5{\cdot}H_2O$:3%Mn^{2+}. (c) Structure diagram of Mn^{2+}-doped host material. (d) Tauc plot of $Cs_2ScCl_5{\cdot}H_2O$.

© Science China Press 2024

are attributed to Mn $2p_{3/2}$ and $2p_{1/2}$, respectively, demonstrating that all Mn ions are present in the sample in the +2 valence form [33–35]. The results of the elemental analysis further prove the successful doping of Mn^{2+} in the host material, which corroborates with the EDS results. Moreover, comparing the high-resolution spectra of Cs and Sc for the doped and undoped samples (Fig. S4), we found that the characteristic peaks of these elements slightly shift toward the high binding energy in the doped samples. We speculate that this shift is due to changes in the corresponding bond lengths after the partial substitution of Sc^{3+} by Mn^{2+}, which can be seen in the subsequent structural simulations thus affecting the electron distributions. A schematic of the structure before and after doping is shown in Fig. 2c.

The absorption spectrum of the $Cs_2ScCl_5{\cdot}H_2O$ sample was evaluated to determine the optical band gap and the corresponding absorption peaks, which are displayed in Fig. S5. Two broad absorption peaks at 265 and 380 nm were demonstrated in the absorption of the $Cs_2ScCl_5{\cdot}H_2O$ sample, which are similar to those reported in previous work [24]. The corresponding Tauc diagram is shown in Fig. 2d. The optical band gap of the substrate was calculated to be ~4.15 eV, which can be corroborated by the subsequently calculated band gap. The UV–vis absorption spectra of the Mn^{2+}-doped samples show broad absorption regions at 430 and 500–600 nm, which can be attributed to the $^6A_1$ to $^4A_1$, ^4E, and $^6A_1$ to $^4T_2$ transitions of the octahedral Mn^{2+}. Cross-referencing the absorption spectra with the spectra of the PL excitation (PLE) of the samples can be used to investigate the excitation properties of the samples.

The optical properties of the samples were assessed to investigate the origin of the fluorescence. The PL and PLE spectra of the host material are shown in Fig. S6, which exhibit broad emission peaks covering almost all the visible regions, similar to that reported previously [24]. Broadband emission of the substrate material is accompanied by an octahedron of 150 nm and a corresponding Stokes shift of ~245 nm. Such broadband emissions and large Stokes shifts often originate from self-trapped exciton (STE) emissions due to strong electron–phonon coupling in the perovskite structure. The lifetime of the substrate material at a monitored wavelength of 560 nm is shown to be 6.62 μs in Fig. S7. This long lifetime is considered in conjunction with the broadband emission and large Stokes shift, indicating that the source of the luminescence is the STE emission rather than, for example, the free exciton emission. The PL spectra of different concentrations are shown in Fig. S8, where the best intensity was obtained at a dopant concentration of 3%; therefore, the sample with 3% dopant concentration was chosen for the later tests. In contrast, the PL emission spectrum of the sample doped with Mn^{2+} is shown in Fig. 3a, which exhibits a quite different emission peak from that of the base material, with a peak of 648 nm in the red region and an FWHM of ~75 nm. Meanwhile, the sample's PLE spectrum was assessed for monitoring the red luminescence (648 nm) to contrast with the absorption, as shown in Fig. 3b. The excitation broadband at 200–300 nm is considered to be a charge transfer from Cl^- to Mn^{2+} [35]. The excitation peaks at 300–550 nm correspond to

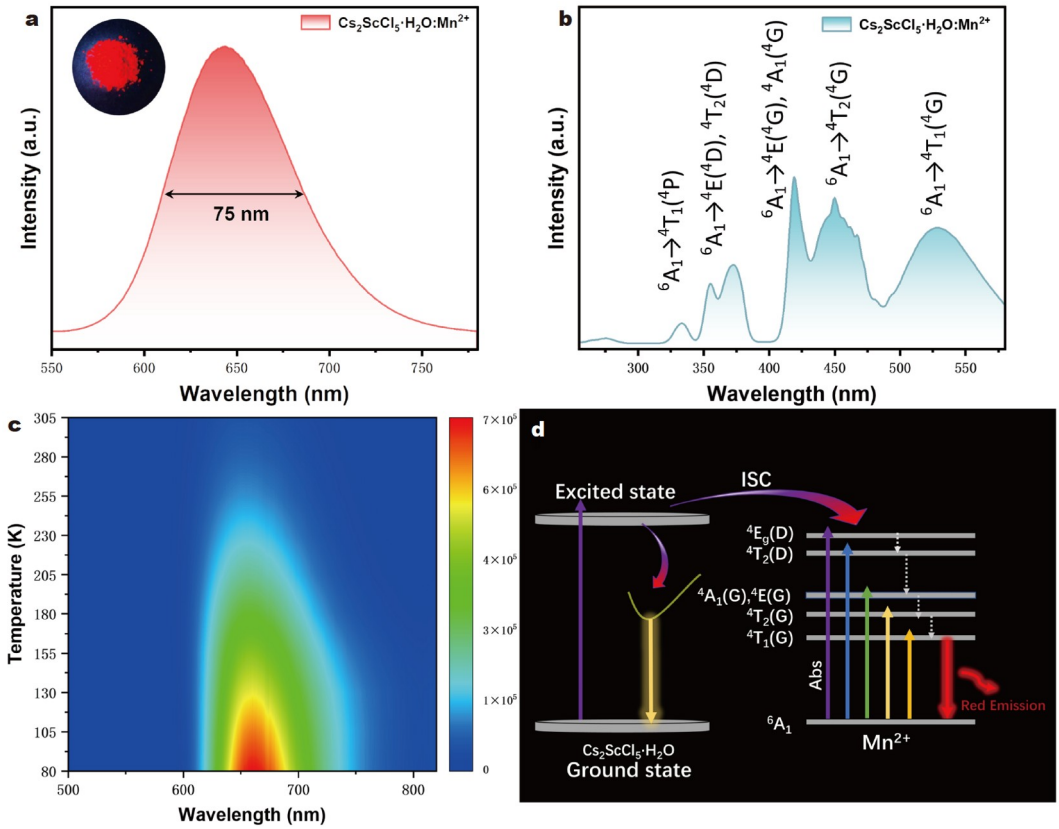

Figure 3 (a) PL spectrum of $Cs_2ScCl_5{\cdot}H_2O$:3%Mn^{2+} with an excitation wavelength of 420 nm (inset: an image of $Cs_2ScCl_5{\cdot}H_2O$:Mn^{2+} under UV light). (b) Excitation spectrum (monitored at 650 nm) of $Cs_2ScCl_5{\cdot}H_2O$:3%Mn^{2+}. (c) Temperature-dependent PL mapping of $Cs_2ScCl_5{\cdot}H_2O$:Mn^{2+} microcrystals under an excitation wavelength of 450 nm. (d) Diagram of energy levels of $Cs_2ScCl_5{\cdot}H_2O$:Mn^{2+}.

© Science China Press 2024

the electronic transitions from the ground state to the different excited states due to the six-coordination of Mn^{2+}, and the specific energy levels are shown in the figure [31,36]. The emission at ~650 nm is from the transition of $^4T_1(^4G)$ to $^6A_1(^6S)$ from the 6-coordination Mn^{2+}. The wavelength-dependent fluorescence and PLE spectra of the sample were measured, as shown in Fig. S9. Because of its constant peak position and similar peak pattern, it is further demonstrated that the fluorescence emission of the sample comes from the excited state of Mn^{2+} and not from surface or lattice defects [37]. Moreover, we can clearly observe the emission originating from the matrix material at ~500 nm when the excitation wavelength is shorter than 400 nm, whereas similar emissions are not observed at excitation wavelengths longer than 400 nm, a finding that is consistent with the absorption in the host material being less than 400 nm and unable to be excited by longer wavelengths. We also found weak STE emission belonging to the substrate material, similar to previous reports [38]. The emission region of the substrate material and the excitation region of Mn^{2+} were found to overlap, and an efficient energy transfer from the host material to the Mn octahedron is highly probable. To further prove the existence of energy transfer, the lifetime of the 550 nm emission peak (emission from the substrate material) was evaluated at undoped and different Mn^{2+} doping concentrations (Fig. S10). The emission peak lifetime decreased considerably from 6.62 to 4.8 μs, which also proves the existence of energy transfer.

To further investigate the origin of the optical performance of the sample, we performed temperature-dependent PL tests in the range of 80–305 K, as shown in Fig. 3c. Among them, we found that the intensity of the sample continually decreased with increasing temperature, which can be attributed to the temperature-quenching phenomenon generated by the pyrolysis of excitons due to the enhanced interaction between excitons and phonons caused by high temperature [39,40]. Moreover, with increasing temperature, there was a blue shift in the fluorescence peak, which is displayed in Fig. S11. This could be due to the decrease in the crystal field intensity owing to the lattice expansion caused by heat [41,42]. By analyzing these optical properties, the optical function of the host material with the dopant ions in the sample is depicted in Fig. 3d. The octahedral Mn^{2+} exists as an important newly introduced emission center with a $^4T_{1g}/^6A_{1g}$ transition, which leads to a strong emission in the red-light region. Absorption in the host material can further increase the exciton density of Mn^{2+} through the exciton transfer process between octahedra, thus enhancing the PLQY. Low doses of Mn^{2+} doping also effectively solve the low luminescence problem of the forbidden region transition in pure Mn-based materials.

To further investigate the band gap and density of states (DOS) of the material, DFT was applied for calculating $Cs_2ScCl_5{\cdot}H_2O$ and $Cs_2ScCl_5{\cdot}H_2O{:}Mn^{2+}$. The band gaps for the host material and the doped sample are shown in Fig. 4a, b, respectively. For the host material, the calculated band gap was

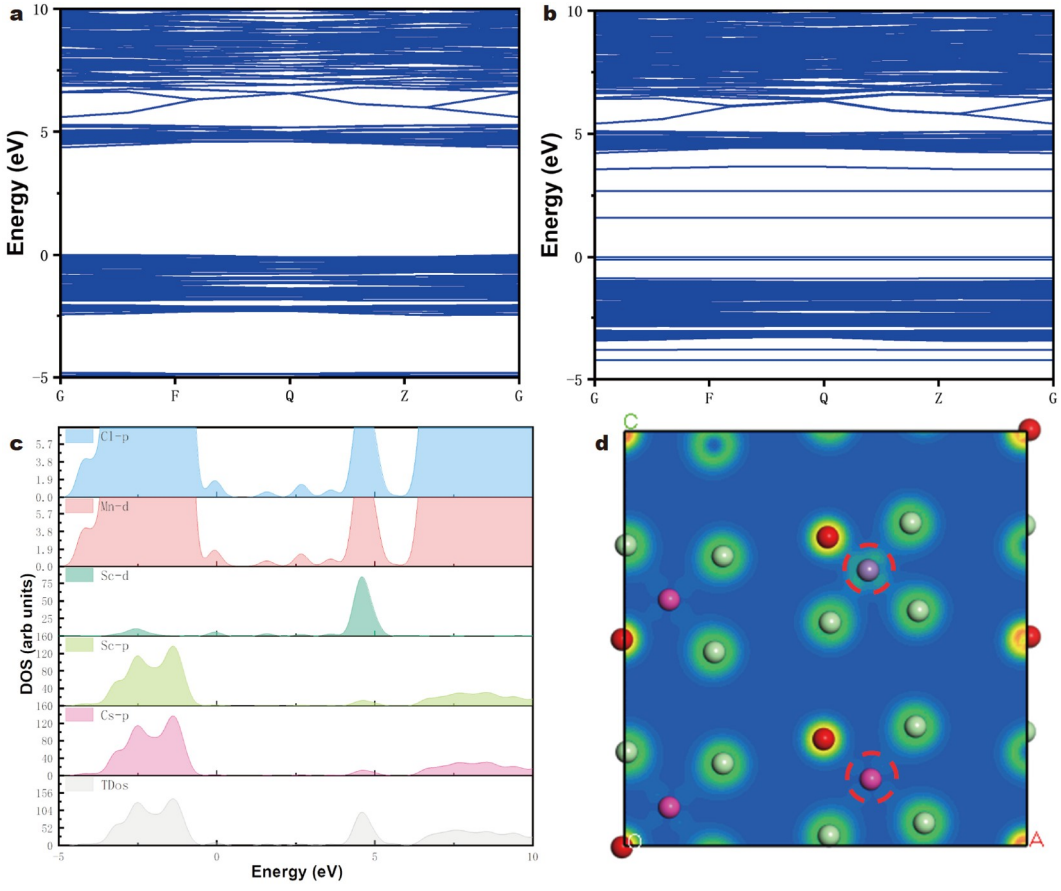

Figure 4 Calculated band structures of (a) $Cs_2ScCl_5{\cdot}H_2O$ and (b) $Cs_2ScCl_5{\cdot}H_2O{:}Mn^{2+}$. (c) Calculated PDOS of $Cs_2ScCl_5{\cdot}H_2O{:}Mn^{2+}$. (d) Charge density isosurface of $Cs_2ScCl_5{\cdot}H_2O{:}Mn^{2+}$ (gray, Mn; pink, Sc).

© Science China Press 2024

~4.3 eV, which was in good agreement with the optical band gap obtained from absorption calculations. The band gap of the doped sample was reduced because of the change in the electronic structure of the material caused by the entry of Mn^{2+} into the lattice. The partial DOS (PDOS) of the sample is shown in Fig. 4c and Fig. S12 for the composition of the valence band maximum (VBM) and conduction band minimum (CBM) as well as the orbital hybridization between the atoms. In this case, the main components of the VBM are the 3d orbitals of Mn, 3d orbitals of Sc, and 3p orbitals of Cl. There are also orbital hybridizations based on Mn, Sc, and Cl, which are very favorable for energy transfer. The CBM primarily consists of the 3p orbitals of Cl and 3d orbitals of Mn. Moreover, the band-gap reduction of the doped sample is primarily due to the doping of Mn^{2+}. The addition of Mn^{2+} leads to the formation of new hybridized orbitals and a new independent state induced by the contribution of the Mn 3d orbital. The relatively high charge density around the host element in the Mn octahedron compared with the Sc octahedron is due to the valence difference between Mn^{2+} and Sc^{3+} (Fig. 4d). With the calculated band gap and other relevant information, the light-absorbing host material can effectively transfer the absorbed excitons into the Mn octahedron, effectively increasing the exciton density, which can thus effectively enhance the PLQY.

The stability issue has been one of the biggest obstacles to the practical application of perovskites. Moreover, the stability of the structure directly affects the optical properties. Therefore, it is necessary to study the stability of the material [43–45]. To explore the stability of the structure at high temperatures, the temperature-dependent XRD pattern is shown in Fig. S13. All the XRD spectra corresponded to the simulated XRD patterns, and there were no new diffraction peaks or notable changes in intensity, indicating that the structure of the samples had good stability in the tested interval. The stability of the optical properties of the sample after high-temperature treatment was also assessed, as shown in Fig. S14. After the high-temperature treatment, the peak position and peak shape of the sample did not change considerably. The intensity decreased relatively, and there was a minor loss, indicating that the sample has good high-temperature resistance. It was not enough to discuss the stability of temperature alone; we also exposed the samples to air to investigate the response of the samples to atmospheric water and oxygen. We studied the XRD patterns (Fig. 5a) and fluorescence spectra (Fig. S15) of samples placed for 1, 3, and 6 months. The XRD patterns showed no notable changes in the samples and no new diffraction peaks were observed, indicating that the placement for 6 months did not cause the samples to deteriorate. The normalized fluorescence spectra profiles show that the emission peak positions and peak shapes are essentially the same, with no shifts, and the corresponding intensity reduction is limited, with ~85% of the fluorescence intensity remaining after 6 months. This indicates that the loss of sample performance is limited and that the structure remains undamaged after 6 months of exposure to air, demonstrating the excellent stability of the material. The PLQY of the samples after 6 months of storage was also assessed to demonstrate the stability of the samples, and the PLQY values remained almost unchanged (Fig. S16).

The excellent red emission performance and structural stability of the material lay a solid foundation for the future application of white LEDs (WLEDs). Physical images of the excellent optical performance are shown in Fig. 5b. The prepared powder material was mixed with commercial phosphor ($Y_3Al_5O_{12}:Ce^{3+}$, Ga^{3+}) and fixed on a blue-light chip using UV structural adhesives. A blue-light chip emitting at 450 nm was used as the excitation source. Under a test current of 20 mA, the fluorescence spectrum of the LED and a picture of the object are shown in Fig. 5c, where the peak covers the entire visible light region from 400 to 800 nm. The CIE color coordinates corresponding to the luminescence peak of the device are (0.339, 0.351), which is in the white-light region, as shown in Fig. 5e. The correlated

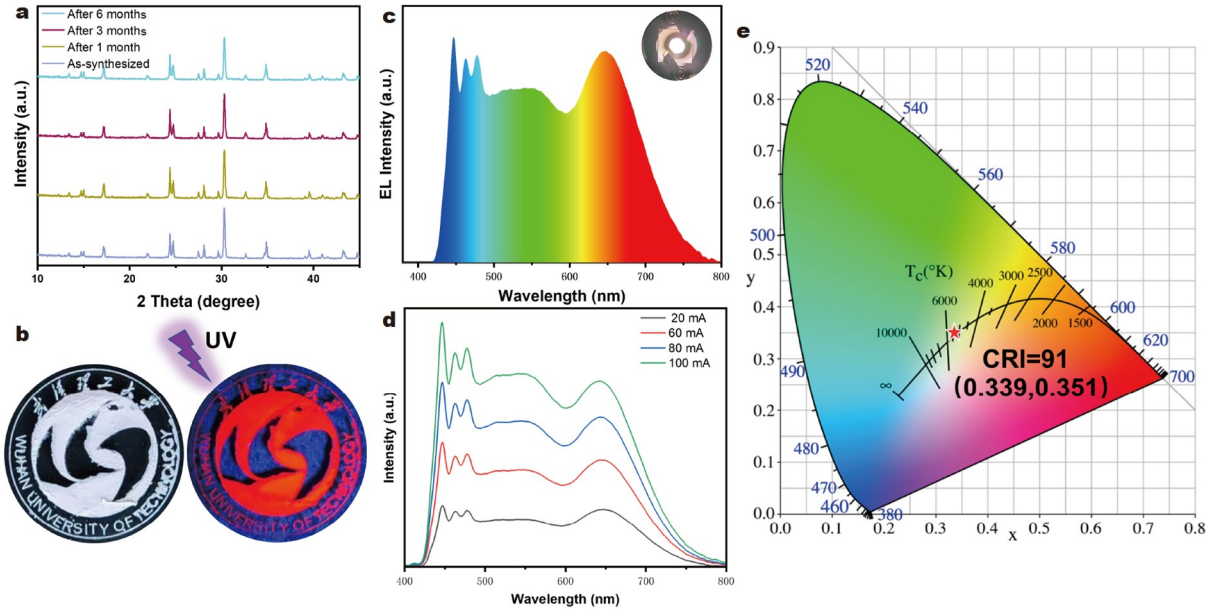

Figure 5 (a) Powder XRD patterns of fresh $Cs_2ScCl_5{\cdot}H_2O$:3%Mn^{2+} and after 1, 3, and 6 months of storage. (b) Physical images under natural light and UV irradiation at 365 nm. (c) Emission spectrum of a WLED prepared from $Cs_2ScCl_5{\cdot}H_2O$:3%Mn^{2+} and commercial phosphor ($Y_3Al_5O_{12}:Ce^{3+}$,Ga^{3+}) under a test current of 20 mA. (d) Emission spectra of the WLED at different test currents. (e) CRI and CIE chromaticity coordinates of the WLED under a test current of 20 mA.

© Science China Press 2024

color temperature and the color rendering index (CRI) of LED devices driven by a 20-mA current are 5207 K and 91, respectively, indicating that the device emits cold white light. Moreover, the excellent CRI proves that the color development of the device is particularly good, and the color reduction degree of the object is far higher than the relevant requirements (CRI > 80). The emission spectrum of the device under different current drives was also assessed to explore the stability of the device (Fig. 5d). Because a high current will induce a higher temperature in the chip, it is a test for the stability of the phosphor. However, even when the current is six times higher than the standard current, the emission spectrum of the device does not collapse, which proves that the device has good stability. These LED results demonstrate the enormous potential $Cs_2ScCl_5{\cdot}H_2O:Mn^{2+}$ samples can achieve in the lighting field, making them favorable candidates for commercial phosphors.

CONCLUSIONS

Herein, we introduced Mn^{2+} into the all-inorganic perovskite structure of $Cs_2ScCl_5{\cdot}H_2O$ using a facile preparation method that allows the rapid synthesis of samples in a short time and under conventional conditions. The QY of the sample (12%) was more than 12 times higher than that of the base material (less than 1%) and nearly 24 times higher than that of $CsMnCl_3{\cdot}2H_2O$ (~0.5%). DFT calculations were applied to study the band-gap properties of the material. Experiments show that the excitons are more effectively confined in the $[MnCl_6]^{4-}$ octahedra, which are separated by the octahedra of the substrate material, thereby enhancing the PLQY. Moreover, the doping of Mn^{2+} added new Mn ion–related hybridized orbitals in the forbidden band region of the host material, which is favorable for the utilization of energy. The host material can be excited by the near-UV or even blue region after doping with Mn^{2+} compared with only absorbing energy in the deep-UV region, which increases the range of applications. Thus, $Cs_2ScCl_5{\cdot}H_2O:Mn^{2+}$ and commercial yellow–green phosphors ($Y_3Al_5O_{12}:Ce^{3+}$ and Ga^{3+}) were mixed in a blue chip (450 nm) to prepare an efficient WLED, demonstrating an excellent CRI of 91. This study also provides innovative ideas for the subsequent easy preparation of high-performance all-inorganic perovskites using simple reagents. Moreover, the combined theoretical and experimental analysis provides new thinking for the exploration of optical properties, and it is hoped that all-inorganic perovskites with high stability and excellent optical properties will have great application prospects.

Received 26 November 2023; accepted 24 January 2024; published online 7 March 2024

1 Akin S, Akman E, Sonmezoglu S. $FAPbI_3$-based perovskite solar cells employing hexyl-based ionic liquid with an efficiency over 20% and excellent long-term stability. Adv Funct Mater, 2020, 30: 2002964
2 Liu S, Yang B, Chen J, *et al.* Efficient thermally activated delayed fluorescence from all-inorganic cesium zirconium halide perovskite nanocrystals. Angew Chem Int Ed, 2020, 59: 21925–21929
3 Li Z, Rao Z, Li Q, *et al.* $Cs_2Zr_{1-x}Te_xCl_6$ perovskite microcrystals with ultrahigh photoluminescence quantum efficiency of 79.46% for high light efficiency white light emitting diodes. Adv Opt Mater, 2021, 9: 2100804
4 Zhang Y, Ma Y, Wang Y, *et al.* Lead-free perovskite photodetectors: Progress, challenges, and opportunities. Adv Mater, 2021, 33: 2006691
5 Yin H, Chen J, Guan P, *et al.* Controlling photoluminescence and photocatalysis activities in lead-free $Cs_2Pt_xSn_{1-x}Cl_6$ perovskites *via* ion substitution. Angew Chem Int Ed, 2021, 60: 22693–22699
6 Zhu X, Du M, Feng J, *et al.* High-efficiency perovskite solar cells with imidazolium-based ionic liquid for surface passivation and charge transport. Angew Chem Int Ed, 2021, 60: 4238–4244
7 Peng X, Yang X, Liu D, *et al.* Targeted distribution of passivator for polycrystalline perovskite light-emitting diodes with high efficiency. ACS Energy Lett, 2021, 6: 4187–4194
8 Li M, Zhao C, Wang Z, *et al.* Interface modification by ionic liquid: A promising candidate for indoor light harvesting and stability improvement of planar perovskite solar cells. Adv Energy Mater, 2018, 8: 1801509
9 Rao Z, Cao M, Chen Z, *et al.* Understanding and effective tuning of red-to-green upconversion emission in Ho-based halide double perovskite microcrystals. Adv Funct Mater, 2024, 34: 2311568
10 Liu C, Fang Z, Sun J, *et al.* Imidazolium ionic liquid as organic spacer for tuning the excitonic structure of 2D perovskite materials. ACS Energy Lett, 2020, 5: 3617–3627
11 Caprioglio P, Cruz DS, Caicedo-Dávila S, *et al.* Bi-functional interfaces by poly(ionic liquid) treatment in efficient pin and nip perovskite solar cells. Energy Environ Sci, 2021, 14: 4508–4522
12 Xu J, Cui J, Yang S, *et al.* Unraveling passivation mechanism of imidazolium-based ionic liquids on inorganic perovskite to achieve near-record-efficiency $CsPbI_2Br$ solar cells. Nano-Micro Lett, 2021, 14: 7
13 Luo H, Huang Y, Liu H, *et al.* Ionic liquid assisted pure blue emission $CsPbBr_3$ quantum dots with improved optical properties and alkyl chain regulated stability. Chem Eng J, 2022, 430: 132790
14 Li Z, Deng Z, Johnston A, *et al.* Precursor tailoring enables alkylammonium tin halide perovskite phosphors for solid-state lighting. Adv Funct Mater, 2022, 32: 2111346
15 Zhou B, Liu Z, Fang S, *et al.* Efficient white photoluminescence from self-trapped excitons in Sb^{3+}/Bi^{3+}-codoped $Cs_2NaInCl_6$ double perovskites with tunable dual-emission. ACS Energy Lett, 2021, 6: 3343–3351
16 Yan S, Tian W, Chen H, *et al.* Synthesis of 0D manganese-based organic-inorganic hybrid perovskite and its application in lead-free red light-emitting diode. Adv Funct Mater, 2021, 31: 2100855
17 Chen B, Guo Y, Wang Y, *et al.* Multiexcitonic emission in zero-dimensional $Cs_2ZrCl_6:Sb^{3+}$ perovskite crystals. J Am Chem Soc, 2021, 143: 17599–17606
18 Tan Z, Li J, Zhang C, *et al.* Highly efficient blue-emitting Bi-doped Cs_2SnCl_6 perovskite variant: Photoluminescence induced by impurity doping. Adv Funct Mater, 2018, 28: 1801131
19 Hoang MT, Pham ND, Yang Y, *et al.* A facile, environmentally friendly synthesis of strong photo-emissive methylammonium lead bromide perovskite nanocrystals enabled by ionic liquids. Green Chem, 2020, 22: 3433–3440
20 Khan SU, Khan WU, Khan WU, *et al.* Eu^{3+}, Sm^{3+} deep-red phosphors as novel materials for white light-emitting diodes and simultaneous performance enhancement of organic–inorganic perovskite solar cells. Small, 2020, 16: 2001551
21 Kong Q, Yang B, Chen J, *et al.* Phase engineering of cesium manganese bromides nanocrystals with color-tunable emission. Angew Chem Int Ed, 2021, 60: 19653–19659
22 Luo Z, Liu Y, Liu Y, *et al.* Integrated afterglow and self-trapped exciton emissions in hybrid metal halides for anti-counterfeiting applications. Adv Mater, 2022, 34: 2200607
23 Feng S, Ma Y, Wang S, *et al.* Light/force-sensitive 0D lead-free perovskites: From highly efficient blue afterglow to white phosphorescence with near-unity quantum efficiency. Angew Chem Int Ed, 2022, 61: e202116511
24 Zhang R, Xu X, Mao X, *et al.* Excitation-dependent emission in all-inorganic lead-free $Cs_2ScCl_5{\cdot}H_2O$ perovskite crystals. Laser Photonics Rev, 2022, 16: 2100689
25 Zhu D, Zaffalon ML, Zito J, *et al.* Sb-doped metal halide nanocrystals: A 0D *versus* 3D comparison. ACS Energy Lett, 2021, 6: 2283–2292
26 Saeki K, Fujimoto Y, Koshimizu M, *et al.* Comparative study of scintillation properties of Cs_2HfCl_6 and Cs_2ZrCl_6. Appl Phys Express, 2016, 9: 042602
27 Artem'ev AV, Davydova MP, Berezin AS, *et al.* New approach toward

 © Science China Press 2024

dual-emissive organic–inorganic hybrids by integrating Mn(II) and Cu(I) emission centers in ionic crystals. ACS Appl Mater Interfaces, 2022, 14: 31000–31009
28 Hu G, Xu B, Wang A, *et al.* Stable and bright pyridine manganese halides for efficient white light-emitting diodes. Adv Funct Mater, 2021, 31: 2011191
29 Zhang W, Thapa S, Sun Y, *et al.* Substitution of Pb with Mn^{2+}/Nd^{3+} to improve the luminescence and thermal stability of Cs_4PbBr_6. Chem Eng J, 2021, 423: 130186
30 Dutta SK, Dutta A, Das Adhikari S, *et al.* Doping Mn^{2+} in single-crystalline layered perovskite microcrystals. ACS Energy Lett, 2019, 4: 343–351
31 Xiao H, Dang P, Yun X, *et al.* Solvatochromic photoluminescent effects in all-inorganic manganese(II)-based perovskites by highly selective solvent-induced crystal-to-crystal phase transformations. Angew Chem Int Ed, 2021, 60: 3699–3707
32 Hao X, Liu H, Ding W, *et al.* Zn^{2+}-doped lead-free $CsMnCl_3$ nanocrystals enable efficient red emission with a high photoluminescence quantum yield. J Phys Chem Lett, 2022, 13: 4688–4694
33 Anthony AM, Pandian MK, Pandurangan P, *et al.* Zero- and one-dimensional lead-free perovskites for photoelectrochemical applications. ACS Appl Mater Interfaces, 2022, 14: 29735–29743
34 Yan J, Zhang S, Wei Q, *et al.* Stoichiometry-controlled phase engineering of cesium bismuth halides and reversible structure switch. Adv Opt Mater, 2022, 10: 2101406
35 Han JH, Viswanath NSM, Park YM, *et al.* Zero-thermal-quenching layered metal halide perovskite. Chem Mater, 2022, 34: 5690–5697
36 Zhu Y, Liang Y, Liu S, *et al.* Narrow-band green-emitting $Sr_2MgAl_{22}O_{36}$:Mn^{2+} phosphors with superior thermal stability and wide color gamut for backlighting display applications. Adv Opt Mater, 2019, 7: 1801419
37 Li K, Ye Y, Zhang W, *et al.* Ultra-stable and color-tunable manganese ions doped lead-free cesium zinc halides nanocrystals in glasses for light-emitting applications. Nano Res, 2022, 15: 9368–9376
38 Wei JH, Liao JF, Wang XD, *et al.* All-inorganic lead-free heterometallic $Cs_4MnBi_2CCl_{12}$ perovskite single crystal with highly efficient orange emission. Matter, 2020, 3: 892–903
39 Su B, Han K, Xia Z. Mn^{2+}-doped Cs_2ZnBr_4 scintillator for X-ray imaging. J Mater Chem C, 2023, 11: 8052–8061
40 Su Y, Yuan L, Wang B, *et al.* Lanthanide-doped Mn^{2+}-based perovskite-like single crystals: Switching on highly thermal-stable near-infrared emission and LED device. J Colloid Interface Sci, 2022, 624: 725–733
41 Huang Y, Pan Y, Guo S, *et al.* Large spectral shift of Mn^{2+} emission due to the shrinkage of the crystalline host lattice of the hexagonal $CsCdCl_3$ crystals and phase transition. Inorg Chem, 2022, 61: 8356–8365
42 Li Z, Li B, Liu W, *et al.* Doping Mn^{2+} in a new layered halide double perovskite $PPA_4NaInCl_8$ ($PPA^+ = C_6H_5(CH_2)_3NH_3^+$): Dimensional reduction accelerating Mn^{2+} dissolution and separation for efficient light emission. Adv Opt Mater, 2023, 11: 2203031
43 Zhang Y, Zhang Z, Yu W, *et al.* Lead-free double perovskite $Cs_2AgIn_{0.9}Bi_{0.1}Cl_6$ quantum dots for white light-emitting diodes. Adv Sci, 2021, 9: 2102895
44 Liu Y, Jing Y, Zhao J, *et al.* Design optimization of lead-free perovskite $Cs_2AgInCl_6$:Bi nanocrystals with 11.4% photoluminescence quantum yield. Chem Mater, 2019, 31: 3333–3339
45 Zhang R, Wang Z, Xu X, *et al.* All-inorganic rare-earth halide double perovskite single crystals with highly efficient photoluminescence. Adv Opt Mater, 2021, 9: 2100689

Acknowledgements This work was supported by the National Natural Science Foundation of China (21774098) and the "111" project (B18038).

Author contributions Gong X conceived and supervised the project; Cao M conducted the experiments and wrote the draft of the manuscript; Li R participated in the discussion and test of the data. All the authors participate in the general discussion.

Conflict of interest The authors declare that they have no conflict of interest.

Supplementary information Supporting data are available in the online version of the paper.

Mengyan Cao is a PhD candidate at Wuhan University of Technology, China, under the supervision of Prof. Xiao Gong and Prof. Xiujian Zhao. Her research focuses on the preparation and optical properties of lead-free luminescent materials.

Renfu Li received his BSc degree (2005) from Xiamen University. He received his MS degree (2017) from Fuzhou University. He is a senior lab master at Fujian Institute of Research on the Structure of Matter, Chinese Academy of Sciences. His research focuses on the optical properties of organic and inorganic luminescent materials, including AIEs, lanthanide ions-doped nanocrystals, lead halide perovskite and lead-free halide perovskites.

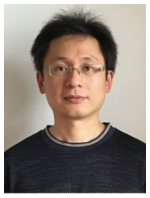

Xiao Gong is a professor at the State Key Laboratory of Silicate Materials for Architectures, Wuhan University of Technology, China. He received his PhD degree in materials science from Zhejiang University. Prior to joining Wuhan University of Technology, he was a postdoctoral associate at the University of Pittsburgh, USA. He is in the Editorial Advisory Board of *Langmuir*. His current research focuses on polymer composite films, functional nanomaterials, the synthesis and application of the fluorescent materials.

Mn^{2+}离子掺杂制备的高效红光发射无铅铯铕卤化物钙钛矿晶体

曹梦妍[1], 李仁富[2*], 李智霖[1], 赵修建[1], 龚晓[1*]

摘要 通过简便的湿化学方法, 将Mn^{2+}离子掺杂到$Cs_2ScCl_5{\cdot}H_2O$钙钛矿中, 可以快速合成具有高光致发光量子产率的钙钛矿晶体. 在红光区掺杂Mn^{2+}的钙钛矿晶体的量子产率比主体材料高出12倍以上, 比$CsMnCl_3{\cdot}2H_2O$高出近24倍. 此外, 利用密度泛函理论计算研究了材料的轨道杂化性质, 进一步研究了材料的光学性质. Mn^{2+}掺杂后, 被Sc八面体分离的Mn八面体可以更有效地限制激子, 有利于提高量子产率. 与原来的带隙相反, 出现了归属于Mn和宿主元素的新杂化轨道. 掺杂样品的吸收和激发范围从深紫外吸收扩展到紫外和可见吸收. 基于上述性质, 利用掺杂Mn^{2+}的钙钛矿制备了蓝芯片激发的高效白色发光二极管, 其显色指数高达91, 为未来在光电子领域的应用开辟了道路.

 © Science China Press 2024